Greening of the brown-dwarf desert

(Article begins on next page)

06 August 2024

Greening of the Brown Dwarf Desert[⋆]

EPIC 212036875b – a 51 M_J object in a 5 day orbit around an F7 V star

Carina M. Persson[1], Szilárd Csizmadia[2], Alexander J. Mustill[3], Malcolm Fridlund[1, 4], Artie P. Hatzes[5],
Grzegorz Nowak[6, 7], Iskra Georgieva[1], Davide Gandolfi[8], Melvyn B. Davies[3], John H. Livingston[9], Enric Palle[6, 7],
Pilar Montañes Rodríguez[6, 7], Michael Endl[10], Teruyuki Hirano[11], Jorge Prieto-Arranz[6, 7], Judith Korth[12],
Sascha Grziwa[12], Massimiliano Esposito[5], Simon Albrecht[13], Marshall C. Johnson[14], Oscar Barragán[8, 15],
Hannu Parviainen[6, 7], Vincent Van Eylen[16], Roi Alonso Sobrino[6, 7], Paul G. Beck[6, 7, 17], Juan Cabrera[2], Ilaria Carleo[18],
William D. Cochran[10], Fei Dai[16, 19], Hans J. Deeg[6, 7], Jerome P. de Leon[9], Philipp Eigmüller[2], Anders Erikson[2],
Akai Fukui[20], Lucía González-Cuesta[6, 7], Eike W. Guenther[5], Diego Hidalgo[6, 7], Maria Hjorth[13], Petr Kabath[21],
Emil Knudstrup[13], Nobuhiko Kusakabe[20, 22], Kristine W. F. Lam[23], Mikkel N. Lund[13], Rafael Luque[6, 7],
Savita Mathur[6, 7], Felipe Murgas[6, 7], Norio Narita[6, 9, 20, 22, 24], David Nespral[6, 7], Prajwal Niraula[25],
A. O. Henrik Olofsson[1], Martin Pätzold[12], Heike Rauer[2, 23], Seth Redfield[18], Ignasi Ribas[26, 27], Marek Skarka[21, 28],
Alexis M. S. Smith[2], Jan Subjak[21, 29], and Motohide Tamura[9, 20, 22]

(Affiliations can be found after the references)

ABSTRACT

Context. Although more than 2 000 brown dwarfs have been detected to date, mainly from direct imaging, their characterisation is difficult due to their faintness and model dependent results. In the case of transiting brown dwarfs it is, however, possible to make direct high precision observations.

Aims. Our aim is to investigate the nature and formation of brown dwarfs by adding a new well-characterised object, in terms of its mass, radius and bulk density, to the currently small sample of less than 20 transiting brown dwarfs.

Methods. One brown dwarf candidate was found by the KESPRINT consortium when searching for exoplanets in the *K2* space mission Campaign 16 field. We combined the *K2* photometric data with a series of multi-colour photometric observations, imaging and radial velocity measurements to rule out false positive scenarios and to determine the fundamental properties of the system.

Results. We report the discovery and characterisation of a transiting brown dwarf in a 5.17 day eccentric orbit around the slightly evolved F7 V star EPIC 212036875. We find a stellar mass of 1.15 ± 0.08 $M_\odot$, a stellar radius of 1.41 ± 0.05 $R_\odot$, and an age of 5.1 ± 0.9 Gyr. The mass and radius of the companion brown dwarf are 51 ± 2 M_J and 0.83 ± 0.03 R_J, respectively, corresponding to a mean density of 108^{+15}_{-13} g cm^{-3}.

Conclusions. EPIC 212036875b is a rare object that resides in the brown dwarf desert. In the mass-density diagram for planets, brown dwarfs and stars, we find that all giant planets and brown dwarfs follow the same trend from ~ 0.3 M_J to the turn-over to hydrogen burning stars at ~ 73 M_J. EPIC 212036875b falls close to the theoretical model for mature H/He dominated objects in this diagram as determined by interior structure models, as well as the empirical fit. We argue that EPIC 212036875b formed via gravitational disc instabilities in the outer part of the disc, followed by a quick migration. Orbital tidal circularisation may have started early in its history for a brief period when the brown dwarf's radius was larger. The lack of spin–orbit synchronisation points to a weak stellar dissipation parameter ($Q'_\star \gtrsim 10^8$) which implies a circularisation timescale of $\gtrsim 23$ Gyr, or suggests an interaction between the magnetic and tidal forces of the star and the brown dwarf.

Key words. Planetary systems – Stars: fundamental parameters – Stars:individual: EPIC 212036875 – Techniques: photometric – Techniques: radial velocity

1. Introduction

The dividing line between gaseous giant planets (GPs) and brown dwarfs (BDs) is still unclear largely due to the lack of well-characterised objects in this mass range. BDs have classically been regarded as objects in between large planets and low-mass stars. Their masses have been defined to be in the range $13 - 80$ M_J (Burrows et al. 2001), sustaining deuterium burning through nuclear fusion for typically 0.1 million yrs, but be-

low the ignition limit of hydrogen at $75 - 80$ M_J. Objects with masses above 65 M_J also burn lithium. The exact limits depend on models and internal chemical composition (Dieterich et al. 2014; Spiegel et al. 2011; Baraffe et al. 2002). Another division between GPs and BDs is based on formation: BDs are considered to form like stars from gravitational instability on a dynamical timescale with the elemental abundance of the interstellar medium, while GPs form on a longer timescale by core accretion with an enhanced metal abundance as compared to their host star (Chabrier et al. 2014). By this definition, the mass domains are overlapping since the minimum BD mass is about 3 M_J, and the maximum planet mass can be as high as tens of M_J. Others argue that BDs should not be distinguished from hydrogen-burning stars as they have more similarities to stars than planets

arXiv:1906.05048v2 [astro-ph.EP] 13 Jun 2019

(Whitworth 2018). Hatzes & Rauer (2015), on the other hand, suggested that BDs should be classified as GPs instead of a separate class of its own based on the mass-density relationship. They defined objects within a mass range of $\sim 0.3 - 60\ M_J$ as the gaseous planet sequence, in analogy with the main sequence of stars. Objects below and above these limits were considered to be low-mass planets and low-mass stars, respectively, although the upper limit could be as high as 80 M_J. This was corroborated by Chen & Kipping (2017) who found that BDs follow the same trend as GPs in the mass-radius diagram up to 80 M_J.

Although more than 2 000 BDs have been detected (e.g. Skrzypek et al. (2016), Johnston 2015[1]) mainly by large-scale direct imaging surveys, most of the detected BDs are free-floating, and only about 400 are found in bound systems at large distances from the primary star. Close BD companions to a main sequence star are very rare. Several surveys have showed that BDs in close orbits (< 3 AU) around main sequence FGKM stars have a much lower frequency than GPs and close binaries (e.g. Marcy & Butler 2000; Grether & Lineweaver 2006; Sahlmann et al. 2011). This is commonly referred to as the BD desert and may be a consequence of different formation mechanisms for low- and high-mass BDs. BDs with masses $35 \lesssim M \sin i \lesssim 55\ M_J$ and orbital periods less than 100 days may represent the driest part of this desert (Ma & Ge 2014). For objects in very close orbits, $a < 0.2$ AU, Triaud et al. (2017) found a paucity of lower masses, $3 - 13\ M_J$.

It is evident that many more well-characterised BDs are required to solve these issues. Characterisation from imaging is, however, difficult since the objects are very faint, unless they are very young, and is heavily dependent on evolutionary models. In the case of eclipsing BDs the situation is different since accurate determination of diameters is possible with photometric observations of the host star. Mass measurements are also relatively easy to perform with high precision due to the high masses of BDs. It is therefore possible to perform a model-independent characterisation of individual BDs found by transit surveys combined with follow-up radial velocity (RV) measurements.

Space-based photometry allows excellent photometric precision and long uninterrupted observations (Fridlund 2018; Deleuil & Fridlund 2018; Borucki 2018). This technique has successfully been utilised to detect thousands of transiting exoplanets by the space missions *CoRoT*, *Kepler* and its extension *K2*. The recently launched *TESS* mission is expected to increase this number even further. The first discovery of a transiting BD, CoRoT-3b (Deleuil et al. 2008), was in fact made from space. The BD sample has since grown with additional detections from space, and also with the ground-based surveys SuperWASP, HATNet, MEarth, and KELT. The sample of well-characterised objects with masses between ∼10 and 80 M_J in bound systems is still, however, very small. Many more are needed to investigate possible differences between GPs and BDs. Using the classic 13 M_J limit between GPs and BDs, only 17 transiting BDs in bound systems around main sequence stars are known today. A summary of 11 BDs, five candidates, and two eclipsing BD binaries is found in Table III.6.1 of Csizmadia (2016). Later discoveries of six additional BDs have been made from space: Kepler-503 b (Cañas et al. 2018), EPIC 219388192 b (Nowak et al. 2017), EPIC 201702477 b (Bayliss et al. 2017), and from the ground: WASP-128 b (Hodžić et al. 2018), LP 261-75 b (Irwin et al. 2018), and HATS-70 b (Zhou et al. 2019).

Table 1: Basic parameters for EPIC 212036875[a].

Parameter	Value
Main Identifiers	
EPIC	212036875
2MASS	J08584567+2052088
WISE	J085845.66+205208.4
TYC	1400-1873-1
UCAC	555-045746
GAIA DR2	684893489523382144
Equatorial coordinates	
α(J2000.0)	$08^h\ 58^m\ 45\overset{s}{.}67$
δ(J2000.0)	$+20°\ 52'\ 08\overset{''}{.}78$
Magnitudes	
B (Johnson)	11.654 ± 0.113
V (Johnson)	10.950 ± 0.095
G (Gaia)	10.9148 ± 0.0009
Kepler	10.937
g	12.257 ± 0.050
r	10.918 ± 0.060
i	10.800 ± 0.070
J	10.042 ± 0.022
H	9.843 ± 0.024
K	9.774 ± 0.018
Parallax (mas)	3.238 ± 0.048
Systemic velocity (km s^{-1})	-22.7 ± 1.7
μ_{RA} (mas yr^{-1})	-2.62 ± 0.08
μ_{Dec} (mas yr^{-1})	-29.70 ± 0.05

Notes. [a] From the Ecliptic Plane Input Catalogue (EPIC; Huber et al. 2016) http://archive.stsci.edu/k2/epic/search.php and the Gaia DR2 archive http://gea.esac.esa.int/archive/.

In this paper we report the independent discovery and observations of EPIC 212036875b performed by the KESPRINT consortium. (e.g. Hjorth et al. 2019; Korth et al. 2019; Livingston et al. 2019; Palle et al. 2019; Gandolfi et al. 2018). EPIC 212036875 was found in the *K2* Campaign 16, and follow-up observations subsequently revealed that the object was the 18th transiting BD detected to date. We note that shortly before submitting this article, Carmichael et al. (2019) publicly announced their discovery and RV observations of EPIC 212036875b. We describe the *K2* photometry in Sect. 2 and the follow-up observations in Sect. 3. We model the star in Sect. 4, and the transit and RVs in Sect. 5. We end the paper with a discussion and conclusions in Sect. 6 and 7, respectively.

2. *K2* photometry and transit detection

Between 7 Dec 2017 and 25 Feb 2018, the *Kepler* space telescope monitored 35 643 objects in the long (29.4 min) cadence mode, and 131 objects with short (1 min) cadence in the direction towards (*J*2000) $\alpha = 08^h54^m50\overset{s}{.}3$ and $\delta = +01°14'06\overset{''}{.}0$ (the *K2* Campaign 16[2]). The data of Campaign 16 was down-

---

[1] http://www.johnstonsarchive.net/astro/browndwarflist.html

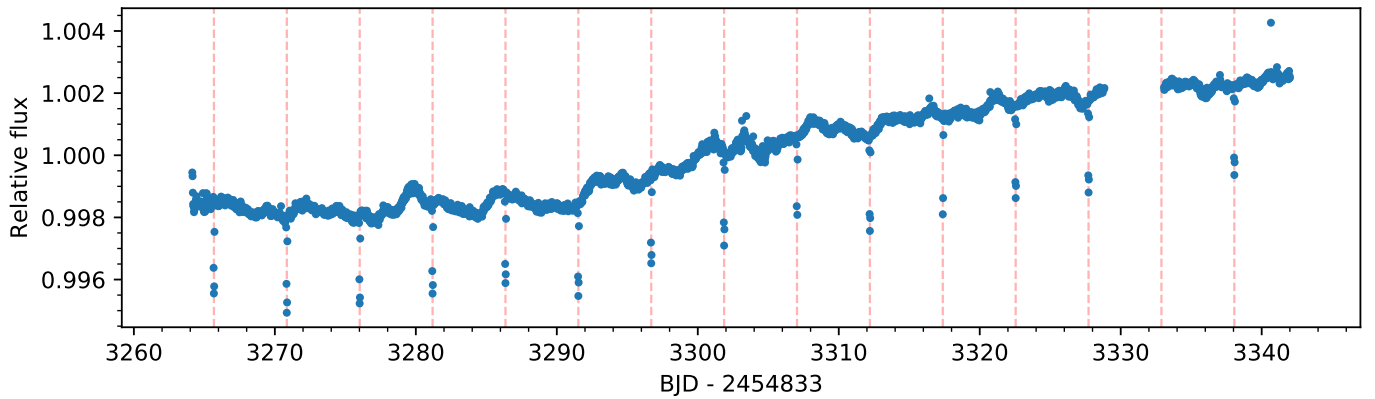[2] https://keplerscience.arc.nasa.gov/k2-data-release-notes.html#k2-campaign-16

Fig. 1: The pre-processed Vanderburg *K2* light curve of EPIC 212036875. The dashed vertical lines mark the 14 narrow and shallow brown dwarf transits used in the analysis. We also mark a missing transit located in a gap of the light curve. The broader periodic variation of approximately 0.07 % is caused by stellar activity.

loaded from the Mikulski Archive for Space Telescopes[3] (MAST). We followed the procedure described in Korth et al. (2019) and searched for periodic signals in the photometric data using the `EXOTRANS` software (Grziwa et al. 2012). The software utilises wavelet-based filters to remove stellar variability and instrument systematics, and a modified BLS (Box-fitting Least Squares; Kovács et al. 2002) algorithm, improved by implementing optimal frequency sampling (Ofir 2014), to detect the most significant transits. Periodic signals were detected in the light curve of the F7 V star EPIC 212036875 with an orbital period of 5.17 days, a mid-transit time T_0 = 3265.68 days (BJD - 2454833), and a depth of $\sim$ 0.4 %. The pre-processed Vanderburg[4] light curve is shown in Fig. 1. The depth is consistent with a Jupiter-sized planet, although the nature of the planet candidate had to await radial velocity follow-up. We found no signs of even-odd depth variations or a secondary eclipse within 1 σ, which is a first step to excluding binaries. We thus proceeded with a follow-up campaign to characterise the EPIC 212036875 system.

The basic parameters of the star are listed in Table 1.

3. Ground-based follow-up

We performed a series of follow-up observations with *(i)* multi-colour photometric observations to rule out eclipsing binary false-positives (Sect. 3.1); *(ii)* reconnaissance spectra observations to remove candidates with rapidly rotating stars, double-lined binaries and blends of spectral components (Sect. 3.2); *(iii)* RV follow-up to obtain the BD mass and co-added spectra needed for stellar spectral modelling (Sect. 3.3); and *(iv)* high resolution adaptive optics (AO; Sect. 3.4) and speckle imaging (Sect. 3.5) to search for contaminant stars that may be background or foreground stars, or physically bounded eclipsing binaries whose light may be diluted by the target star and generate transit-like signals. Speckle and AO observations are fundamentally different techniques; NESSI speckle probes the inner region ($< 0.2''$) around the target star at optical wavelengths, while AO achieves a much higher contrast in the $0.2'' - 1.0''$ region in the near infrared. These regions are not possible to explore with the *K2* data with a sky-projected pixel size of 4''.

3.1. MUSCAT2

We observed a full transit of EPIC 212036875b with MuSCAT2 at the Carlos Sanchez Telescope (TCS) on the night of 3 April 2018. MuSCAT2 is a 4-colour imager that allows for simultaneous observations in *g′*, *r′*, *i′*, and *z′* (Narita et al. 2018). The observations started at 20:15 UT and ended at 23:30 UT, covering the full transit and some pre- and post transit baselines. The night was clear, with variable seeing between 1''and 2''. Exposure times were set to 5 s in all channels.

The differential photometry and transit light curve analysis were carried out with a dedicated MuSCAT2 pipeline. The photometry follows standard aperture photometry practices: we calculated an astrometric solution for each frame using an offline version of astrometry.net (Lang et al. 2010), and retrieved the photometry for a set of comparison stars and aperture sizes.

The transit modelling continued by first choosing a set of optimal apertures that minimise the relative light curve point-to-point scatter. Next, we jointly fitted a transit model with a linear baseline model (a linear model in sky level, airmass, seeing, and CCD position variations) to the four light curves using PyTransit and LDTk (Parviainen 2015; Parviainen & Aigrain 2015). Finally, we swapped the linear baseline model to a Gaussian process-based model with the final kernel consisting of a product of squared exponential kernels for all the covariates, and carried out MCMC sampling to obtain an estimate of the model parameter posterior distribution. The final light curves are shown in Fig. 2. The transit model allows for colour-dependent variations in transit depth due to blending by an unresolved source, and our analysis allows us to rule out any significant contamination that would affect the parameter estimates derived from the transit photometry.

3.2. Reconnaissance spectra with Tull

On 5 April 2018 we obtained a reconnaissance spectrum of EPIC 212036875 with the Tull spectrograph at the 2.7 m telescope at McDonald Observatory. The high-resolution ($R \approx 60\,000$) spectrum was reduced using standard `iraf` routines. We derived a first estimate of the stellar spectroscopic parameters using the code `Kea` (Endl & Cochran 2016): $T_{\rm eff}$ = 6380 ± 58 K, [Fe/H]= −0.21 ± 0.03 dex, $\log(g_\star)$ = 4.25 ± 0.14 (cgs), and $V \sin i_\star$= 11.9 ± 0.3 km s^{-1}.
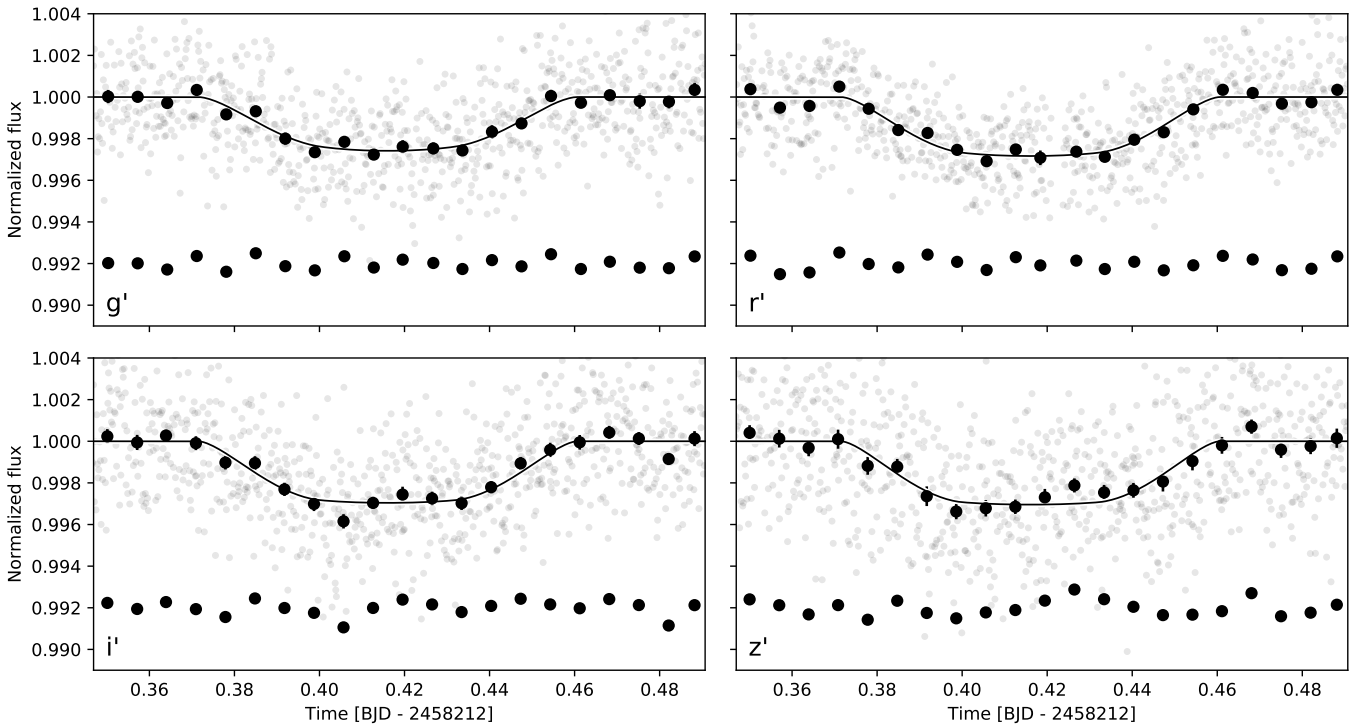

Fig. 2: Transit light curves of EPIC 212036875b obtained with MuSCAT2 (TCS), in *g′* (upper-left), *r′* (upper-right), *i′* (lower-left), and *z′* (lower-right) filters, respectively. The black solid line is the best-fit model accounting for the de-trending and transit components. The residuals are plotted in the lower portion of each respective plot.

We found no evidence of a double-lined binary or any blends of spectral components.

3.3. Radial velocity follow-up with FIES

The RV follow-up was performed with FIES (the FIbre-fed Échelle Spectrograph; Telting et al. 2014; Frandsen & Lindberg 1999) mounted on the 2.56 m Nordic Optical Telescope (NOT) at the Roque de los Muchachos Observatory. We observed nine high-resolution ($R \approx 67\,000$) spectra between 9 April and 22 May 2018 as part of our CAT and TAC programmes 57-015, 57-206, and 57-210, and OPTICON program 2018A-044. To account for the RV offset caused by a major instrument refurbishment that occurred on 30 April 2018, we treated the RV taken between 9 and 26 April, and between 6 and 8 May as two independent data-sets. In addition, 14 intermediate-resolution ($R \approx 47\,000$) FIES spectra were also acquired between 12 May 2018 and 26 Feb 2019, as part of the OPTICON programme 2018B-052 and the Spanish-Nordic programme 58-301. Depending on the sky conditions and scheduling constraints, we set the exposure times to $1800 - 3600$ s for both resolutions. To trace the RV drift of the instrument we followed the strategy outlined in Gandolfi et al. (2015) and Buchhave et al. (2010) and bracketed the science exposures with long-exposed (60–90 s) ThAr spectra. We used the standard IRAF and IDL routines to reduce the data. The S/N ratio of the extracted spectra ranges between ~35 and 75 per pixel at 5500 Å. Radial velocities were extracted via multi-order cross-correlations with the spectrum of the RV standard star HD 168009, for which we adopted an absolute RV of -64.650 km s^{-1}(Udry et al. 1999).

The FIES RVs are listed in Table A.1. Figure A.2 shows the generalised Lomb-Scargle periodogram of the offset-corrected Doppler measurements (combined by subtracting the systemic velocities listed in Table 4). We found a very significant peak at the orbital frequency of the transiting brown dwarf with a false alarm probability FAP $\ll 10^{-6}$, proving that the Doppler reflex motion of the star induced by the orbiting companion is clearly detected in our data.

3.4. Subaru/IRCS AO imaging

In order to obtain high-contrast, high-resolution images of EPIC 212036875, we performed AO imaging with the InfraRed Camera and Spectrograph (IRCS, Kobayashi et al. 2000) atop the Subaru 8.2 m telescope on 14 June 2018. The target star was used as a natural guide and AO correction was applied to obtain high-contrast *K′*-band images of the target. We used the fine-sampling mode (1 pix $\approx$ 21 mas), and implemented a five-point dithering to minimise the impacts of bad pixels and cosmic rays.

We reduced the raw frames with a standard procedure described in (Hirano et al. 2016) to produce an aligned and combined image of EPIC 212036875. The full width at the half maximum of the co-added target image was 0″089 suggesting that the AO correction worked well for this target. As shown in the inset of Fig. 3, EPIC 212036875 exhibits no nearby source. Following Hirano et al. (2018) we estimated the detection limit of possible nearby sources by computing a 5 σ contrast curve drawn in Fig. 3. The achieved contrast is $\Delta m_{K′} > 7$ mag beyond 0″5 from EPIC 212036875.

3.5. NESSI imaging

To further constrain the presence of stellar companions at close separations, we conducted speckle imaging of
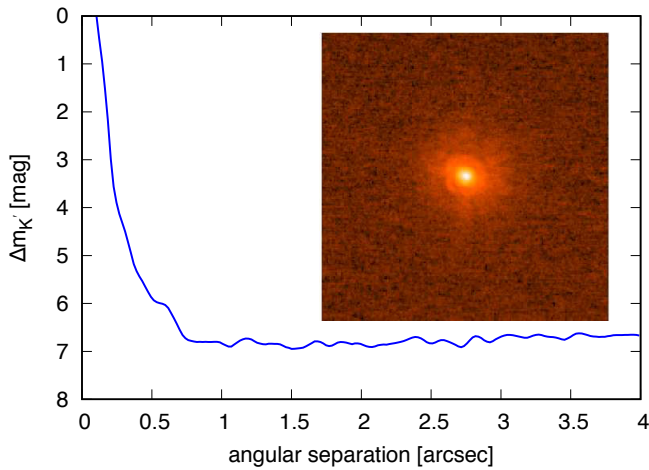
Fig. 3: IRCS/Subaru AO-imaging in the K'-band and 5 σ magnitude contrast curve as a function of angular separation from EPIC 212036875. The inset shows the $16'' \times 16''$ saturated image. Northeast is up and to the left.
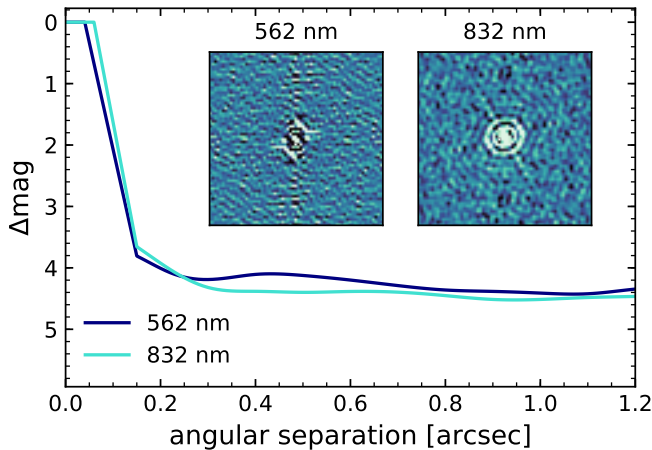

Fig. 4: NESSI/WIYN speckle interferometry reconstructed images in the r- and z-narrowbands and 5 σ contrast curves. The inset images are $1''.2 \times 1''.2$. Northeast is up and to the left.

EPIC 212036875 using the NASA Exoplanet Star and Speckle Imager (NESSI; Scott & Howell 2018) at the WIYN 3.5 m telescope on 19 June 2018 (program ID 2018A-0181). NESSI operates simultaneously in two bands centred at 562 nm (r-narrowband) and 832 nm (z-narrowband). We collected and reduced the data following the procedures described by Howell et al. (2011), yielding $4''.6 \times 4''.6$ reconstructed images of the host star (the inset shows the central $1''.2 \times 1''.2$ in Fig. 4). We did not detect any secondary sources in the reconstructed images. The 5 σ detection limits are shown in Fig. 4; the contrast is approximately 4.5 mag beyond $0''.3$ from EPIC 212036875 in both images.

We used the NESSI and Subaru magnitude limits to estimate limits on companion masses vs. separation and find that massive companions are excluded outside ~100 AU (Fig. A.1).

4. Stellar analysis

4.1. Spectral analysis

Before we modelled the BD, we first computed the absolute mass and radius of the host star. In order to obtain the stellar parameters needed in the stellar models, we used the spectral analysis package SME (Spectroscopy Made Easy; Valenti & Piskunov 1996; Piskunov & Valenti 2017). This software calculates synthetic stellar spectra from grids of atmosphere models which are then fitted to the observations using a χ^2-minimising procedure. Here we specifically used the ATLAS12 model spectra (Kurucz 2013), and SME version 5.22 to model our co-added FIES spectra. We followed well established methods described in Fridlund et al. (2017) and Persson et al. (2018) to compute $T_{\rm eff}$, $\log(g_\star)$, $V \sin i_\star$, and abundances. The micro- and macro-turbulent velocities, $V_{\rm mic}$ and $V_{\rm mac}$, were fixed using the calibration equations for Sun-like stars from Bruntt et al. (2010) and Doyle et al. (2014), respectively. The line lists were taken from the Vienna Atomic Line Database[5] (Ryabchikova et al. 2015).

Our results obtained with SME ($T_{\rm eff} = 6230 \pm 90$ K) are in agreement with the values listed in the Gaia DR2 archive ($T_{\rm eff} = 6227 \pm 100$ K) and EPIC ($T_{\rm eff} = 6336$ K), and are also consistent with the Kea results from the Tull reconnaissance spectra in Sect. 3.2 ($T_{\rm eff} = 6380 \pm 58$ K). The resulting $T_{\rm eff}$ and the luminosity in the Gaia DR2 archive implies a spectral type of F7 V. All final results are listed in Table 2.

4.2. Stellar mass and radius

We used the Southworth (2011) calibration equations to compute the stellar mass and radius. These empirical relations, based on data from eclipsing binaries, are valid for masses up to 3 $M_\odot$ and account for metal abundance and evolution. It provides the advantage of using the stellar density which has a higher precision than $\log(g_\star)$ since it is derived from the the transit light curve. Additional input parameters are $T_{\rm eff}$ and [Fe/H].

We also compared the Southworth results with several other, independent methods. The first is the Torres et al. (2010) calibration equations based on a different set of eclipsing binaries, as well as interferometrically determined stellar diameters. The input parameters are $T_{\rm eff}$, $\log(g_\star)$, and [Fe/H]. We further applied the Bayesian PARAM 1.3[6] model tool tracks (da Silva et al. 2006) with the PARSEC isochrones (Bressan et al. 2012) and the apparent visual magnitude, $T_{\rm eff}$, [Fe/H], and the parallax as input. The derived age and $\log(g_\star)$ from PARAM 1.3 are 5.1 ± 0.9 Gyr and 4.10 ± 0.04 (cgs), respectively. Finally, when we compared the derived mass and radius to a typical F7 V star, we noted that EPIC 212036875 seems to be slightly evolved, in line with a typical life time of about ~ 7 Gyr. EPIC 212036875b is one of only two BDs where the age can be determined relatively precisely, due to its evolutionary state. The other BD with a well determined age is EPIC 219388192b (Nowak et al. 2017) which is a member of Ruprecht 147, the oldest nearby open cluster association.

All models are in excellent agreement with each other. The results from all models are listed in Table 3, and the final adopted stellar parameters are listed in Table 2.

---

[5] http://vald.astro.uu.se
[6] http://stev.oapd.inaf.it/cgi-bin/param_1.3

Table 2: Adopted stellar parameters of EPIC 212036875.

Parameter	EPIC 212036875
Effective temperature $T_{\text{eff}}{}^a$ (K)	6230 ± 90
Surface gravity $\log(g_\star)^{a,\,b}$ (cgs)	4.17 ± 0.10
Metallicity [Fe/H]^a (dex)	-0.28 ± 0.05
Metallicity [Ca/H]^a (dex)	-0.14 ± 0.05
Metallicity [Na/H]^a (dex)	-0.11 ± 0.05
Metallicity [Mg/H]^a (dex)	-0.16 ± 0.05
Rotation velocity $V \sin i_\star{}^{a,c}$ (km s^{-1})	10.8 ± 1.5
Microturbulent V^d (km s^{-1})	1.3
Macroturbulent V^e (km s^{-1})	5.2
Mass $M_\star{}^f$ ($M_\odot$)	1.15 ± 0.08
Radius $R_\star{}^f$ ($R_\odot$)	1.41 ± 0.05
Density $\rho_\star{}^g$ (g cm^{-3})	0.55 ± 0.04
Luminosity $L_\star{}^h$ ($L_\odot$)	$3.01^{+0.05}_{-0.07}$
Spectral type	F7 V
Rotation period^i (days)	7.2 ± 0.5
Age^j (Gyr)	5.1 ± 0.9

Notes. $^{(a)}$ From SME modelling. $^{(b)}$ Modelled using Mg ɪ. The Ca ɪ model gives $\log(g_\star) = 4.20 \pm 0.20$ (cgs). $^{(c)}$ The projected stellar rotation speed of its surface. $^{(d)}$ Fixed with the empirical calibration by Bruntt et al. (2010). $^{(e)}$ Fixed with the empirical calibration by Doyle et al. (2014). $^{(f)}$ Southworth (2011) calibration equation. $^{(g)}$ Density from pyaneti transit modelling in Sect. 5. Density from adopted stellar mass and radius is 0.58 ± 0.08 g cm^{-3}. $^{(h)}$ Gaia DR2 archive. $^{(i)}$ From the generalised Lomb-Scargle periodogram. $^{(j)}$ PARAM 1.3.

Table 3: Stellar mass and radius of EPIC 212036875 as derived from different methods. The typical values for a F7 V star are listed as comparison.

Method	$M_\star$ ($M_\odot$)	$R_\star$ ($R_\odot$)
Southworth^a	1.15 ± 0.08	1.41 ± 0.05
Torres^b	1.19 ± 0.09	1.43 ± 0.29
PARAM 1.3	1.10 ± 0.04	1.52 ± 0.06
Gaia DR2^c	. . .	1.49 ± 0.05
EPIC^d	1.21 ± 0.11	$1.38^{+0.32}_{-0.17}$
Spectral type^e F7 V	1.21	1.30

Notes. $^{(a)}$ Southworth (2011) calibration equations. $^{(b)}$ Torres et al. (2010) calibration equations. $^{(c)}$ Gaia DR2 archive. $^{(d)}$ The K2 Ecliptic Plane Input Catalog. $^{(e)}$ Cox (2000).

4.3. Stellar rotation period

The *K2* light curve of EPIC 212036875 displays periodic and quasi-periodic photometric variations with a semi-amplitude of ∼0.07%. These are superimposed on a long-term photometric trend with a peak-to-peak amplitude of ∼0.4% (Fig. 1), which we attributed to the slow drift often present in *K2* data (Vanderburg & Johnson 2014). Given the spectral type of the host star, the periodic and quasi-periodic variability is likely induced by magnetically active regions carried around by stellar rotation.

We used the generalised Lomb-Scargle (GLS) periodogram (Zechmeister & Kürster 2009) and the auto-correlation function (ACF) method (McQuillan et al. 2014) to estimate the rotation period of the star. Prior to computing the GLS periodogram and the ACF, we masked out the transits and removed the long-term trend by dividing the out-of-transit light curve by the best-fitting 4th-order cubic spline (Fig. A.3, upper panel). The GLS periodogram of the corrected light curve (Fig. A.3, middle panel) shows a very significant peak at $f = 0.14$ d^{-1} ($P_{\text{rot}} = 7.2$ days) with FAP ≪ 10^{-6}, estimated from the bootstrap method (Kuerster et al. 1997). The ACF of the light curve (Fig. A.3, lower panel) shows correlation peaks at ∼7, 14, 21, 28 days. We interpreted the peak at ∼7 days as the rotation period of the star and the peaks at ∼14, 21, and 28 days as its first, second, and third harmonics, respectively. By fitting a Gaussian function to the highest peak of the GLS periodogram, we derived a rotation period of $P_{\text{rot}} = 7.2 \pm 0.5$ days. Assuming that the star is seen almost equator-on ($\sin i_\star \approx 1$), the spectroscopically derived rotational velocity $V \sin i_\star$ and the stellar radius imply a rotation period of 6.6 ± 0.9 days, in very good agreement with our results. The orbital period of the brown dwarf is thus within 7 % to a 3:2 commensurability with the stellar rotation period.

We used the formula from Winn et al. (2007) to constrain $i_\star$ (the inclination of the stellar spin axis relative to the sky plane), and found $\sin i_\star = V \sin i_\star P_{\text{rot}}/(2\pi R_\star) \approx 1.09 \pm 0.17$. The value with $\sin i_\star > 1$ was rejected as unphysical and we determined a lower bound of $i_\star$ to 66° with 1 σ confidence.

Since the $V \sin i_\star$ of EPIC 212036875 is relatively high, the Rossiter-McLaughlin (RM) effect could be measured with current state-of-the-art spectrographs, mounted on 8–10 m class telescopes, using either RV RM or Doppler tomographic methodology. A first order estimate of the amplitude of the RM effect is ∼16 m s^{-1} using the equation $\Delta V = (R_{\text{bd}}/R_\star)^2 \times \sqrt{1 - b^2} \times V \sin i_\star$ (Winn 2010; Triaud 2018). Note, however, that with a large impact parameter the actual amplitude of the RM effect is a strong function of the angle between the sky projections of the stellar spin axis and the orbit normal (λ), implying that the actual RM amplitude could vary substantially from the above estimate.

Apart from the independent measurements of $V \sin i_\star$ and λ, the measurement of the RM effect, together with the P_{rot} and $V \sin i_\star$ measurements to constrain the inclination of the stellar rotation axis, would also allow a constraint upon the misalignment angle, ψ (the 3-D obliquity angle between the stellar spin axis and the orbital axis). Measuring the spin-orbit misalignment of EPIC 212036875b would be valuable because there are only a handful of such measurements available for transiting BDs (Triaud et al. 2009; Siverd et al. 2012; Triaud et al. 2013; Zhou et al. 2019). Furthermore, this object is the only one of these for which the full 3-D spin-orbit angle is measurable, allowing better constraints on the system architecture. Finally, all of the other objects observed to date have circular orbits, unlike EPIC 212036875b; measuring the spin-orbit misalignment will enable a full dynamical characterisation of this system, which will have consequences for our understanding of how the system formed (see Sect. 6.2).

5. Transit and Radial Velocity modelling

We used the well tested and publicly available PYTHON/FORTRAN pyaneti[7] (Barragán et al. 2019) package to carry out simultaneous modelling of both the *K2* light curve
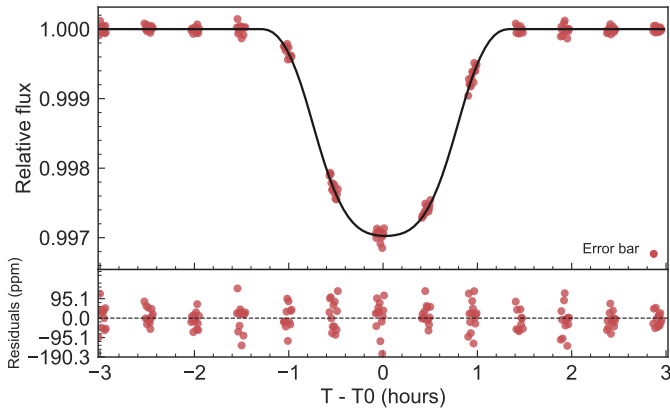
---

[7] https://github.com/oscaribv/pyaneti

Fig. 5: Transit light curve folded to the orbital period of EPIC 212036875b. The *K2* photometric data is indicated with the red points, and the best-fitted transit model with the solid black line. The residuals of the fit are shown in the lower panel.

and the FIES RV measurements. The code uses Markov chain Monte Carlo (MCMC) methods based on Bayesian analysis and has successfully been used by us in e.g. Gandolfi et al. (2019) and Barragán et al. (2018b). In preparation for the modelling, the light curve was detrended with the `exotrending` (Barragán & Gandolfi 2017) code. This procedure reduces the flux variations of any long-term systematic or instrumental trends. Each of the 14 transits was cut out of the light curve, and four hours around each transit were masked to ensure that no in-transit data was used in the process, before fitting a second order polynomial to the remaining out-of-transit data.
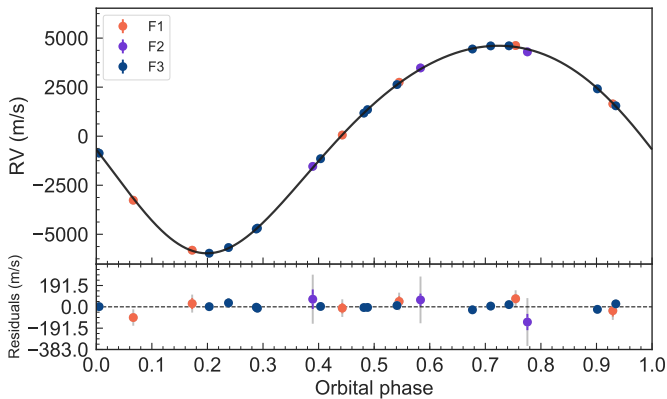

Fig. 6: Radial velocity curve of EPIC 212036875 phase folded to the orbital period of the brown dwarf. The different colours mark the different FIES setups, and the best-fitted RV model is indicated with the solid black line. The residuals of the fit are shown in the lower panel. The coloured error bars are without jitter, and the grey error bars includes the jitter.

Following Barragán et al. (2018a), we fitted a Keplerian orbit to the RV data with an offset term for each systemic velocity from the different instrumental setups. We fitted for the scaled orbital distance ($a/R_\star$), the eccentricity (e), the argument of periastron (ω), the impact parameter ($b = a\cos(i)/R_\star \frac{1-e^2}{1+e\sin(\omega)}$), the Doppler semi-amplitude variation (K), the orbital period (P_{orb}), the mid-transit time (T_0), and the BD-to-star radius ratio ($R_{BD}/R_\star$). We used flat uniform priors over the ranges listed in Table. 4, except for the limb darkening coefficients (LDCs).

Since the observational cadence of *K2* is close to an integer fraction of the orbital period, the data points appear in clumps in the folded light curve in phase space, as shown in Fig. 5. The ingress and egress are not well sampled and the LDCs are poorly constrained by the data. We therefore used Gaussian priors and the Mandel & Agol (2002) quadratic limb darkening equation based on the linear and quadratic coefficients u_1 and u_2, respectively. We used the Kipping (2013) parametrisation $q_1 = (u_1 + u_2)^2$ and $q_2 = 0.5u_1(u_1 + u_2)^{-1}$, and an interpolation[8] of the Claret & Bloemen (2011) limb darkening tables to our spectroscopic parameters and the *Kepler* bandpass to set Gaussian priors to q_1 and q_2. We used conservative 0.1 error bars on both the linear and quadratic coefficients.

To account for the long *K2* integration time of almost 30 minutes, we integrated the transit models over ten steps (Kipping 2010). The parameter space was explored with 500 independent chains randomly created inside the prior ranges. Convergence was checked after every 5 000 iterations and when reached, the last 5 000 iterations were used to create a posterior distribution of 250 000 independent points for every parameter. We removed one outlier from the light curve. Since χ^2/d.o.f = 1.3, we fitted for an RV jitter term for each instrument setup in the model to take into account additional instrumental noise not included in the uncertainties and stellar activity-induced variation, and a light curve jitter term to account for the dispersion of the in- and out-of-transit data to obtain χ^2/d.o.f = 1.0.

The high RV amplitude of about 5 km s^{-1} in Fig. 6 immediately signalled that the mass of the transiting object is much higher than the expected mass from a Jupiter-like planet. This is not possible to derive from the light curve alone since BDs and Jupiters have approximately the same size. The final mass is about 5 % of the stellar host mass. We also note that the BD is near grazing as the derived impact parameter is $0.920^{+0.005}_{-0.006}$ which suggests that the derivation of limb darkening may be less accurate (Csizmadia et al. 2013). If EPIC 212036875 had a typical radius of an F7 V star instead of being slightly evolved (with about 8 % larger radius), the BD would be grazing.

Carmichael et al. (2019) used the TRES spectrograph at the 1.5 m Tillinghast telescope at Mt. Hopkins, Arizona with a spectral resolution $R = 44\,000$ covering $390 - 910$ nm to measure 14 RVs with S/N $\approx 22 - 45$ of EPIC 212036875. This can be compared to our 23 RVs with S/N $\approx 35 - 75$. Their uncertainties are somewhat larger than ours, but our results agree within 1 σ.

The final results are listed in Table 4. We used the median and 68.3 % credible interval of the posterior distributions which all were smooth and unimodal. We show the folded light curve with the best-fitted transit model in Fig. 5, and the phase-folded RV curve with our best-fitted model in Fig. 6.

6. Discussion

EPIC 212036875 is a rare type of object in the BD desert. In this section we will investigate its formation and tidal circularisation in addition to a comparison of GPs and BDs in the mass-density diagram.

6.1. Formation

There are several different paths to form BDs (for a summary see e.g. Whitworth 2018). Objects all the way from stellar

---

[8] http://astroutils.astronomy.ohio-state.edu/exofast/limbdark.shtml (Eastman et al. 2013)

Table 4: Priors to the `pyaneti` model of EPIC 212036875b and results.

Parameter	Units	Priors[a]	Final value
Fitted parameters			
T_0	Transit epoch (BJD$_{TDB}$- 2 450 000).......	$\mathcal{U}$[8098.665, 8098.695]	8098.6791 ± 0.0002
P_{orb}	Orbital period (days)	$\mathcal{U}$[5.1679, 5.1719]	5.16992 ± 0.00002
e	Eccentricity	$\mathcal{U}$[0, 0.3]	0.134 ± 0.002
ω	Argument of periastron (degrees)	$\mathcal{U}$[0, 180]	163 ± 1
b	Impact parameter	$\mathcal{U}$[0, 1]	$0.920^{+0.005}_{-0.006}$
$a/R_\star$	Scaled semi-major axis	$\mathcal{U}$[1.1, 15]	9.2 ± 0.2
$R_{BD}/R_\star$	Scaled brown dwarf radius	$\mathcal{U}$[0, 0.1]	0.0608 ± 0.0009
K	Doppler semi-amplitude variation (km s^{-1})	$\mathcal{U}$[0,15]	5.289 ± 0.013
q_1	Parameterised limb-darkening coefficient .	$\mathcal{G}$[0.38, 0.10]	0.41 ± 0.10
q_2	Parameterised limb-darkening coefficient .	$\mathcal{G}$[0.26, 0.10]	0.26 ± 0.10
Derived Parameters			
M_{BD}	Brown dwarf mass (M_J)................	...	51 ± 2
R_{BD}	Brown dwarf radius (R_J)	...	0.83 ± 0.03
i^b	Inclination (degrees)...................	...	83.9 ± 0.2
a	Semi-major axis (AU)	...	0.060 ± 0.003
F	Insolation ($F_\oplus$).......................	...	740 ± 50
$\rho_\star^c$	Stellar density (g cm^{-3})................	...	0.55 ± 0.04
ρ_{BD}	Brown dwarf density (g cm^{-3})...........	...	108^{+15}_{-13}
$\log(g_{BD})$	Brown dwarf surface gravity (cgs)	...	5.23 ± 0.02
T_{eq}^d	Equilibrium temperature (K)	...	1450 ± 30
T_{14}	Total transit duration (hours)	...	2.17 ± 0.01
T_{23}	Full transit duration (hours)	...	0.76 ± 0.09
u_1	Linear limb-darkening coefficient	...	0.33 ± 0.14
u_2	Quadratic limb-darkening coefficient	...	0.30 ± 0.13
Additional Parameters			
γ_1	Systemic velocity FIES1 (km s^{-1})........	$\mathcal{U}$[-27.1655, -16.5310]	−21.26 ± 0.03
γ_2	Systemic velocity FIES2 (km s^{-1})........	$\mathcal{U}$[-22.9664, -16.9289]	−21.33 ± 0.16
γ_3	Systemic velocity FIES3 (km s^{-1})........	$\mathcal{U}$[-27.3661, -16.5940]	−21.30 ± 0.01
σ_{F1}	RV jitter FIES1 (km s^{-1})...............	$\mathcal{U}$[0, 1]	$0.064^{+0.046}_{-0.030}$
σ_{F2}	RV jitter FIES2 (km s^{-1})...............	$\mathcal{U}$[0, 1]	$0.202^{+0.498}_{-0.129}$
σ_{F3}	RV jitter FIES3 (km s^{-1})...............	$\mathcal{U}$[0, 1]	$0.0092^{+0.010}_{-0.006}$
σ_{tr}	Light curve jitter	$\mathcal{U}$[0, 0.00004733]	0.000025 ± 0.000005

Notes. [a] $\mathcal{U}$[a,b] refers to uniform priors in the range $a - b$, and $\mathcal{G}$[a,b] refers to Gaussian priors with mean a and standard deviation b. [b] Orbit inclination relative to the plane of the sky. [c] Density from pyaneti transit modelling. Density from adopted stellar mass and radius is 0.58 ± 0.08 g cm^{-3}. [d] Assuming isotropic re-radiation and a Bond albedo of zero. Increasing the albedo to e.g. 0,3 and 0.6, we find $T_{eq} \approx 1310$ and 1140 K, respectively.

masses down to about 3 M_J can form through gravitational collapse and turbulent fragmentation like stars (Padoan & Nordlund 2004; Hennebelle & Chabrier 2008). In protoplanetary discs, BDs can also form up to possibly a few tens of M_J according to the core-accretion planet formation theory in either its traditional planetesimal accretion or later pebble accretion variants (e.g. Pollack et al. 1996; Rice & Armitage 2003; Alibert et al. 2004; Lambrechts & Johansen 2012; Mordasini et al. 2012). For EPIC 212036875b with a mass of 51 ± 2 M_J, too massive for formation by core accretion, formation by gravitational instability in the protoplanetary disc may instead be pos-

sible (Toomre 1964; Kratter & Lodato 2016). Disc fragmentation typically occurs at radii >10 AU and forms fragments with initial masses of a few to a few tens of Jupiter masses (see reviews by Kratter & Lodato 2016; Nayakshin 2017). We show in Appendix B and Fig. B.1 that gravitational instability can indeed give rise to fragments with the mass of EPIC 212036875 b. One of these fragments must then migrate to the present orbit of EPIC 212036875 b, which can happen through Type I migration (Baruteau et al. 2011; Malik et al. 2015), although the extent of this is debated in the literature (Stamatellos 2015; Vorobyov & Elbakyan 2018). On the other hand, gravitational instability of-
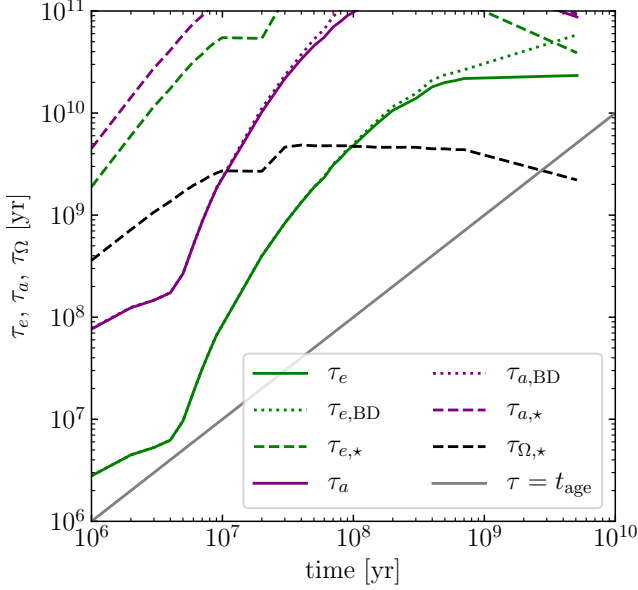
Fig. 7: Timescales for tidal orbital circularisation τ_e, semimajor axis decay τ_a, and stellar spin evolution, $\tau_{\Omega,\star}$. The contributions from the star and the brown dwarf as given by Eqs. 1 – 4 are shown, as well as the net effect, taking quality factors $Q'_\star = 10^8$ and $Q'_{\rm BD} = 10^5$. The diagonal line marks where the timescale at a given age is equal to the system's age.

ten gives rise to more than one fragment, and in this case the dynamical interactions between fragments enhance their migration rate through the disc (Forgan et al. 2018). Indeed, the moderate eccentricity of EPIC 212036875b may be a relic of these dynamical interactions, after some reduction by tidal forces.

6.2. Tidal evolution of the system

As the BD is on a close orbit with non-zero eccentricity, its orbit may be affected by tidal torques. These arise either from the deformation of the BD by the star (henceforth the planetary tide) or from the deformation of the star by the BD (henceforth the stellar tide). These tides cause a change in both orbital semi-major axis and eccentricity, and hence there are four timescales to consider: the contributions of each tide to the decay of the semi-major axis and to the eccentricity. We use the tidal model of Jackson et al. (2008) and define the following timescales τ:

$$\frac{1}{\tau_{a,\star}} = a_{\rm BD}^{-13/2} \frac{9}{2} \sqrt{\frac{G}{M_\star}} \frac{R_\star^5 M_{\rm BD}}{Q'_\star} \tag{1}$$

$$\frac{1}{\tau_{a,{\rm BD}}} = a_{\rm BD}^{-13/2} \frac{63}{2} \sqrt{GM_\star^3} \frac{R_{\rm BD}^5 e_{\rm BD}^2}{Q'_{\rm BD} M_{\rm BD}} \tag{2}$$

$$\frac{1}{\tau_{e,\star}} = a_{\rm BD}^{-13/2} \frac{171}{16} \sqrt{\frac{G}{M_\star}} \frac{R_\star^5 M_{\rm BD}}{Q'_\star} \tag{3}$$

$$\frac{1}{\tau_{e,{\rm BD}}} = a_{\rm BD}^{-13/2} \frac{63}{4} \sqrt{GM_\star^3} \frac{R_{\rm BD}^5}{Q'_{\rm BD} M_{\rm BD}} , \tag{4}$$

where $Q'_\star$ and $Q'_{\rm BD}$ are the tidal quality factors of the star and the BD. We adopt quality factors of 10^8 for the star, in line both with the recent empirical calibration of Collier Cameron & Jar-

dine (2018) for stars in the equilibrium tide regime and with dynamical tide calculations for a 1.2 $M_\odot$ F-type star by Ogilvie & Lin (2007), and 10^5 for the BD as inferred for Jupiter (Lainey et al. 2009). For simplicity, we hold Q constant for both the star and the brown dwarf. In reality, Q can exhibit a complicated dependence on the ratio of the periods of the orbit and of the stellar spin: see Fig. 8 of Barker & Ogilvie (2009). We find that, with the current system parameters, the stellar tide dominates, and the decay timescales are $\tau_a = 87$ Gyr and $\tau_e = 23$ Gyr. These values are longer than the system age, and hence the BD's orbit will not be currently tidally evolving. We note that the preprint of Carmichael et al. (2019) gives a slightly longer circularisation time of 47 Gyr. The difference is largely due to them considering only the tide raised on the brown dwarf.

Note that the tidal timescales given in Eqs. 1 – 4 are extremely strong functions of the physical radii of the BD and of the star, so the tidal timescales change with system age (see, e.g., Zahn & Bouchet 1989; Mathis 2015; Bolmont & Mathis 2016). To explore the historical evolution of the tidal forces, we used the PHOENIX BT-Settl models (Baraffe et al. 2015) to obtain the radii of both the primary and the BD, and calculated the tidal timescales as a function of system age (see Fig. 7). This shows that for the system's main sequence lifetime the tidal forces have been negligible, but that the circularisation timescale was comparable to the system age at ages of a few Myr, when the BD radius was several $R_{\rm J}$. Thus, it is possible that EPIC 212036875 b started tidally circularising early in its history and then stopped as its radius contracted.

A further issue relates to the evolution of the stellar spin: around 98% of the system's angular momentum lies in the brown dwarf's orbit, so it should spin the star up to (pseudo-)synchronisation[9] if the timescale is short enough. For present parameters, pseudo-synchronisation occurs at $\Omega_{\rm rot,ps} = 1.083 \pm 0.003 \Omega_{\rm orb}$, far from the actual value of $(\Omega_{\rm rot,actual}/\Omega_{\rm orb} = 0.69)$. With $Q'_\star = 10^8$ we find a timescale for spin evolution of $\tau_{\Omega,\star} = 2.2$ Gyr, comparable to the system age. Given that the star is not pseudo-synchronised, this implies that $Q'_\star \gtrsim 10^8$. In principle, $Q'_\star$ can be determined by transit timing variations, but this is challenging: from Eq. 7 of Birkby et al. (2014), we estimate that transits would occur just 1 s earlier after 20 years even if $Q'_\star = 10^7$. Alternatively, magnetic effects such as magnetic breaking may force the system away from pseudo-synchronisation: magnetic fields are possessed by both BDs (of kG or stronger: Kao et al. 2018; Berdyugina et al. 2017; Metodieva et al. 2017) and F stars (e.g. Mathur et al. 2014; Augustson et al. 2013). The stellar wind and the magnetism of the BD, studied e.g. in Ferraz-Mello et al. (2015), can also interplay, as well as induction heating (Kislyakova et al. 2018).

We summarise a potential formation and evolution history for this system: EPIC 212036875b formed through gravitational instability early in the protoplanetary disc's evolution. It may have formed as one of several similar objects, the others either ejected by dynamical interactions or undetectable given current data. The interactions with the other objects would have excited EPIC 212036875b's orbital eccentricity, and hastened its migration towards the primary star in the few Myr of the protoplanetary disc's lifetime. At this young age, the BD's large radius may have led to some tidal decay of its orbital eccentricity, but after several Myr its radius would have shrunk enough to weaken tidal forces enough to freeze its orbit in place. Finally, the tide

---

[9] Pseudo-synchronisation occurs for eccentric orbits where the spin angular velocity locks to a value given by Eq. (42) of Hut (1981). The exact value is a function of eccentricity and orbital frequency.
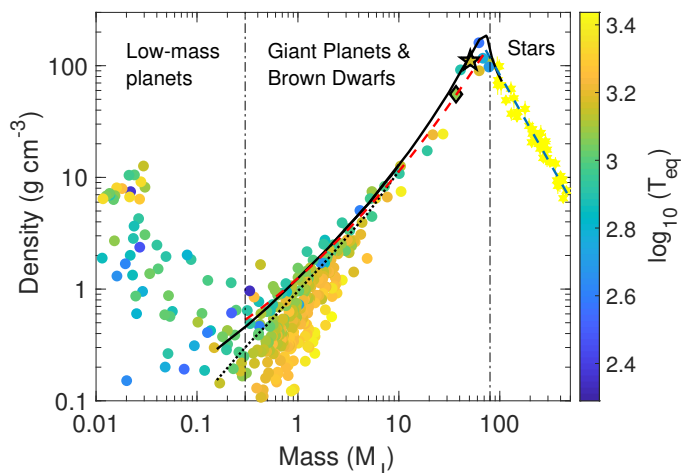
Fig. 8: The mass-density diagram for planets, brown dwarfs, and low-mass stars in eclipsing binaries with a precision in measured mass and density < 20%. The star and diamond symbols mark the locations of EPIC 212036875b and EPIC 219388192b also found by our programme (Nowak et al. 2017). The red dashed line represent a second order polynomial fit to the data with $M = 0.3 - 80 \, M_{\rm J}$ and equilibrium temperatures < 1000 K. The blue dashed line shows a linear fit to the stars with $M > 80 \, M_{\rm J}$. The nominal separation at 80 $M_{\rm J}$ between brown dwarfs and stars, and the empirical separation between low-mass and giant planets at 0.3 $M_{\rm J}$, are marked with the vertical dashed-dotted lines. The solid black line shows the theoretical relationship for H/He dominated giant objects with Z = 0.02, age = 5 Gyr, without irradiation (Baraffe et al. 2003, 2008), and the dotted black line the same model including irradiation from a solar-type star at 0.045 AU (Baraffe et al. 2008).

raised on the star by the BD may have begun forcing the star towards spin-orbit pseudo-synchronisation during the star's main-sequence lifetime, but this process has not yet finished.

6.3. Mass-density diagram

In order to investigate possible differences between BDs and GPs, we show a mass-density diagram in Fig. 8 for planets[10] and BDs[11]. It should be noted that all these objects have close-in orbits to their host star (most have $P_{\rm orb} < 10$ days). Also shown are eclipsing low-mass stars[12] up to 450 $M_{\rm J}$ (0.43 $M_{\odot}$) mostly from ground-based discoveries. We only include objects with a precision in mass and density better than 20 % (in total 253 GPs and BDs, and 43 low-mass stars). The vertical dashed-dotted line at 80 $M_{\rm J}$ marks the nominal separation between BDs and nuclear burning M dwarfs. The colours of the planets and brown dwarfs indicate the logarithm of the equilibrium temperatures, $T_{\rm eq}$. It is clearly seen that low-mass GPs with high incident flux, and thus high $T_{\rm eq}$, have lower densities which could be a sign of in-

---

[10] Well-studied planets listed at `http://www.astro.keele.ac.uk/jkt/tepcat/`.
[11] References in Sect. 1. discovered by space- and ground-based transit searches.
[12] Ribas (2003); Bouchy et al. (2005); Pont et al. (2005, 2006); Demory et al. (2009); Tal-Or et al. (2013); Zhou et al. (2014); Díaz et al. (2014); Chaturvedi et al. (2016) and references in Table 1; Gillen et al. (2017); von Boetticher et al. (2017); Shporer et al. (2017); Chaturvedi et al. (2018) and references in Table 4; Carmichael et al. (2019).

flated radii due to the proximity to the host stars (Miller & Fortney 2011; Baraffe et al. 2014; Tremblin et al. 2017). We fitted a second order polynomial to the data (red dashed line) between 0.3 $M_{\rm J}$ and 80 $M_{\rm J}$ for objects with $T_{\rm eq} < 1000$ K to exclude objects with inflated radii (Weiss et al. 2013), in total 33 objects, and found $\log \rho = 0.16 \times \log^2(M) + 0.80 \times \log(M) + 0.10$. The blue dashed line shows a linear fit to the stars with $M > 80 \, M_{\rm J}$: $\log(\rho) = -1.6 \times \log(M) + 5.1$. Compared to Hatzes & Rauer (2015), we now find a sharp turn-over at $\sim 73 \, M_{\rm J}$ instead of $\sim 60 \, M_{\rm J}$. The empirical fit follows closely the theoretical relationship for H/He dominated GPs (Baraffe et al. 2008) and BDs (Baraffe et al. 2003) with Z = 0.02, age = 5 Gyr and without irradiation drawn with a solid black line. The dotted black line shows the same model including irradiation from a solar-type star at $a = 0.045$ AU (Baraffe et al. 2008) which clearly shows the impact of irradiation for the lower mass GPs. At the lower end, we find a turn-over at $\sim 0.3 \, M_{\rm J}$ in agreement with Hatzes & Rauer (2015), marking the transition to low-mass planets. Our results are in agreement with Chen & Kipping (2017) who found $R \sim M^{-0.04}$ for objects between 0.4 $M_{\rm J}$ and 80 $M_{\rm J}$.

Our two BDs fall close to the theoretical model for H/He dominated BDs as well as the empirical fit. No distinguishing features between GPs and BDs can be seen. After a brief phase lasting ~10 Myr when the deuterium and lithium fusion halts contraction, BDs cool and contract in a way similar to GPs. This suggests that both types of objects will follow the same trend in the mass-density diagram independent of the formation mechanism, especially at late ages. At earlier stages, the difference in radius is larger (e.g. Baraffe et al. 2008) and contributes to the scatter of the data points.

7. Conclusions

We report the discovery and characterisation of a rare object with a mass of 51 ± 2 $M_{\rm J}$ and a radius of 0.83 ± 0.03 $R_{\rm J}$ in an eccentric 5.17 day orbit around the slightly evolved F7 V star EPIC 212036875. Since the star is seen close to equator-on, future observations with large 8–10 m class telescopes, could allow the measurement of the (3-D) obliquity angle between the stellar rotation axis and the brown dwarf orbit axis via the Rossiter-McLaughlin effect. Thanks to the evolutionary state of the host star, this is one of the few transiting brown dwarfs for which a relatively precise age can be estimated. Our results are in agreement with Carmichael et al. (2019) who recently reported an independent discovery and characterisation of EPIC 212036875b.

We show with a simple analytical model that formation of a brown dwarf of the required mass is possible at several tens of AU through gravitational instability, although significant orbital migration is required to bring the object to its current orbit. The orbit may have experienced a period of tidal circularisation within the first few Myr of the system's life when the brown dwarf's radius was very much larger than it is at present, which ceased as its physical radius contracted. The stellar spin may have been affected by the tidal torque from the BD during the system's main-sequence lifetime, but the lack of spin–orbit synchronisation points to a weak stellar dissipation parameter ($Q'_{\star} \gtrsim 10^8$). There is also a possibility that magnetic field plays a role here which could change this estimate.

We find no distinction between brown dwarfs and giant planets based on the mass-density diagram. This supports the previous suggestion by Hatzes & Rauer (2015), and supported by Chen & Kipping (2017), that BDs could simply represent the high mass end of GPs and that there are no observable differences between mature BDs and GPs. The BD desert may be a

reflection of the decreasing number of objects towards the high mass end of the GP distribution formed by core-accretion, and the low-mass end of stars formed by gravitational instabilities.

References

Alibert, Y., Mordasini, C., & Benz, W. 2004, A&A, 417, L25
Augustson, K. C., Brun, A. S., & Toomre, J. 2013, The Astrophysical Journal, 777, 153
Baraffe, I., Chabrier, G., Allard, F., & Hauschildt, P. H. 2002, A&A, 382, 563
Baraffe, I., Chabrier, G., & Barman, T. 2008, A&A, 482, 315
Baraffe, I., Chabrier, G., Barman, T. S., Allard, F., & Hauschildt, P. H. 2003, A&A, 402, 701
Baraffe, I., Chabrier, G., Fortney, J., & Sotin, C. 2014, Protostars and Planets VI, 763
Baraffe, I., Homeier, D., Allard, F., & Chabrier, G. 2015, A&A, 577, A42
Barker, A. J. & Ogilvie, G. I. 2009, MNRAS, 395, 2268
Barragán, O. & Gandolfi, D. 2017, Exotrending: Fast and easy-to-use light curve detrending software for exoplanets, Astrophysics Source Code Library
Barragán, O., Gandolfi, D., & Antoniciello, G. 2019, MNRAS, 482, 1017
Barragán, O., Gandolfi, D., Dai, F., et al. 2018a, A&A, 612, A95
Barragán, O., Gandolfi, D., Smith, A. M. S., et al. 2018b, MNRAS, 475, 1765
Baruteau, C., Meru, F., & Paardekooper, S.-J. 2011, MNRAS, 416, 1971
Bayliss, D., Hojjatpanah, S., Santerne, A., et al. 2017, AJ, 153, 15
Berdyugina, S. V., Harrington, D. M., Kuzmychov, O., et al. 2017, ApJ, 847, 61
Birkby, J. L., Cappetta, M., Cruz, P., et al. 2014, MNRAS, 440, 1470
Bolmont, E. & Mathis, S. 2016, Celestial Mechanics and Dynamical Astronomy, 126, 275
Borucki, W. J. 2018, Space Missions for Exoplanet Science: Kepler/K2, 80
Bouchy, F., Pont, F., Melo, C., et al. 2005, A&A, 431, 1105
Brandeker, A. & Cataldi, G. 2019, A&A, 621, A86
Bressan, A., Marigo, P., Girardi, L., et al. 2012, MNRAS, 427, 127
Bruntt, H., Bedding, T. R., Quirion, P.-O., et al. 2010, MNRAS, 405, 1907
Buchhave, L. A., Bakos, G. Á., Hartman, J. D., et al. 2010, ApJ, 720, 1118

Burrows, A., Hubbard, W. B., Lunine, J. I., & Liebert, J. 2001, Reviews of Modern Physics, 73, 719
Cañas, C. I., Bender, C. F., Mahadevan, S., et al. 2018, ApJ, 861, L4
Carmichael, T., Latham, D., & Vanderburg, A. 2019, arXiv e-prints [arXiv:1903.03118]
Chabrier, G., Johansen, A., Janson, M., & Rafikov, R. 2014, Protostars and Planets VI, 619
Chaturvedi, P., Chakraborty, A., Anandarao, B. G., Roy, A., & Mahadevan, S. 2016, MNRAS, 462, 554
Chaturvedi, P., Sharma, R., Chakraborty, A., Anandarao, B. G., & Prasad, N. J. S. S. V. 2018, AJ, 156, 27
Chen, J. & Kipping, D. 2017, ApJ, 834, 17
Claret, A. & Bloemen, S. 2011, A&A, 529, A75
Collier Cameron, A. & Jardine, M. 2018, MNRAS, 476, 2542
Cox, A. N. 2000, Allen's astrophysical quantities
Csizmadia, S. 2016, III.6 Exploration of the brown dwarf regime around solar-like stars by CoRoT, ed. CoRot Team, 143
Csizmadia, S., Pasternacki, T., Dreyer, C., et al. 2013, A&A, 549, A9
da Silva, L., Girardi, L., Pasquini, L., et al. 2006, A&A, 458, 609
Deleuil, M., Deeg, H. J., Alonso, R., et al. 2008, A&A, 491, 889
Deleuil, M. & Fridlund, M. 2018, CoRoT: The First Space-Based Transit Survey to Explore the Close-in Planet Population, 79
Demory, B.-O., Ségransan, D., Forveille, T., et al. 2009, A&A, 505, 205
Díaz, R. F., Montagnier, G., Leconte, J., et al. 2014, A&A, 572, A109
Dieterich, S. B., Henry, T. J., Jao, W.-C., et al. 2014, AJ, 147, 94
Doyle, A. P., Davies, G. R., Smalley, B., Chaplin, W. J., & Elsworth, Y. 2014, MNRAS, 444, 3592
Eastman, J., Gaudi, B. S., & Agol, E. 2013, PASP, 125, 83
Endl, M. & Cochran, W. D. 2016, PASP, 128, 094502
Ferraz-Mello, S., Tadeu dos Santos, M., Folonier, H., et al. 2015, ApJ, 807, 78
Fletcher, M., Nayakshin, S., Stamatellos, D., et al. 2019, arXiv e-prints [arXiv:1901.08089]
Forgan, D. H., Hall, C., Meru, F., & Rice, W. K. M. 2018, MNRAS, 474, 5036
Frandsen, S. & Lindberg, B. 1999, in Astrophysics with the NOT, ed. H. Karttunen & V. Piirola, 71
Fridlund, M. 2018, Space Missions for Exoplanet Research: Overview and Introduction, 77
Fridlund, M., Gaidos, E., Barragán, O., et al. 2017, A&A, 604, A16
Gandolfi, D., Barragán, O., Livingston, J. H., et al. 2018, A&A, 619, L10
Gandolfi, D., Fossati, L., Livingston, J. H., et al. 2019, ApJ, 876, L24
Gandolfi, D., Parviainen, H., Deeg, H. J., et al. 2015, A&A, 576, A11
Gillen, E., Hillenbrand, L. A., David, T. J., et al. 2017, ApJ, 849, 11
Gramajo, L. V., Rodón, J. A., & Gómez, M. 2014, AJ, 147, 140
Grether, D. & Lineweaver, C. H. 2006, ApJ, 640, 1051
Grziwa, S., Pätzold, M., & Carone, L. 2012, MNRAS, 420, 1045
Hatzes, A. P. & Rauer, H. 2015, ApJ, 810, L25
Hennebelle, P. & Chabrier, G. 2008, ApJ, 684, 395
Hirano, T., Dai, F., Gandolfi, D., et al. 2018, AJ, 155, 127
Hirano, T., Fukui, A., Mann, A. W., et al. 2016, ApJ, 820, 41
Hjorth, M., Justesen, A. B., Hirano, T., et al. 2019, MNRAS, 484, 3522
Hodžić, V., Triaud, A. H. M. J., Anderson, D. R., et al. 2018, MNRAS, 481, 5091
Howell, S. B., Everett, M. E., Sherry, W., Horch, E., & Ciardi, D. R. 2011, AJ, 142, 19
Huber, D., Bryson, S. T., Haas, M. R., et al. 2016, ApJS, 224, 2
Hut, P. 1981, A&A, 99, 126
Ida, S., Guillot, T., & Morbidelli, A. 2016, A&A, 591, A72
Irwin, J. M., Charbonneau, D., Esquerdo, G. A., et al. 2018, AJ, 156, 140
Jackson, B., Greenberg, R., & Barnes, R. 2008, ApJ, 678, 1396
Kao, M. M., Hallinan, G., Pineda, J. S., Stevenson, D., & Burgasser, A. 2018, ApJS, 237, 25
Kipping, D. M. 2010, MNRAS, 408, 1758
Kipping, D. M. 2013, MNRAS, 435, 2152
Kislyakova, K. G., Fossati, L., Johnstone, C. P., et al. 2018, ApJ, 858, 105
Kobayashi, N., Tokunaga, A. T., Terada, H., et al. 2000, in Proc. SPIE, Vol. 4008, Optical and IR Telescope Instrumentation and Detectors, ed. M. Iye & A. F. Moorwood, 1056–1066
Korth, J., Csizmadia, S., Gandolfi, D., et al. 2019, MNRAS, 482, 1807
Kovács, G., Zucker, S., & Mazeh, T. 2002, A&A, 391, 369
Kratter, K. & Lodato, G. 2016, ARA&A, 54, 271
Kuerster, M., Schmitt, J. H. M. M., Cutispoto, G., & Dennerl, K. 1997, A&A, 320, 831
Kupka, F. G., Ryabchikova, T. A., Piskunov, N. E., Stempels, H. C., & Weiss, W. W. 2000, Baltic Astronomy, 9, 590
Kurucz, R. L. 2013, ATLAS12: Opacity sampling model atmosphere program, Astrophysics Source Code Library
Lainey, V., Arlot, J.-E., Karatekin, Ö., & van Hoolst, T. 2009, Nature, 459, 957
Lambrechts, M. & Johansen, A. 2012, A&A, 544, A32
Lang, D., Hogg, D. W., Mierle, K., Blanton, M., & Roweis, S. 2010, Astron. J., 139, 1782
Livingston, J. H., Dai, F., Hirano, T., et al. 2019, MNRAS, 484, 8

Ma, B. & Ge, J. 2014, MNRAS, 439, 2781

Malik, M., Meru, F., Mayer, L., & Meyer, M. 2015, ApJ, 802, 56

Mandel, K. & Agol, E. 2002, ApJ, 580, L171

Marcy, G. W. & Butler, R. P. 2000, PASP, 112, 137

Mathis, S. 2015, A&A, 580, L3

Mathur, S., García, R. A., Ballot, J., et al. 2014, A&A, 562, A124

McQuillan, A., Mazeh, T., & Aigrain, S. 2014, ApJS, 211, 24

Metodieva, Y. T., Kuznetsov, A. A., Antonova, A. E., et al. 2017, MNRAS, 465, 1995

Miller, N. & Fortney, J. J. 2011, ApJ, 736, L29

Mordasini, C., Alibert, Y., Georgy, C., et al. 2012, A&A, 547, A112

Narita, N., Fukui, A., Kusakabe, N., et al. 2018, arXiv e-prints [arXiv:1807.01908]

Nayakshin, S. 2017, PASA, 34, e002

Nowak, G., Palle, E., Gandolfi, D., et al. 2017, AJ, 153, 131

Ofir, A. 2014, A&A, 561, A138

Ogilvie, G. I. & Lin, D. N. C. 2007, ApJ, 661, 1180

Padoan, P. & Nordlund, Å. 2004, ApJ, 617, 559

Palle, E., Nowak, G., Luque, R., et al. 2019, A&A, 623, A41

Parviainen, H. 2015, MNRAS, 450, 3233

Parviainen, H. & Aigrain, S. 2015, MNRAS, 453, 3822

Persson, C. M., Fridlund, M., Barragán, O., et al. 2018, A&A, 618, A33

Piskunov, N. & Valenti, J. A. 2017, A&A, 597, A16

Pollack, J. B., Hubickyj, O., Bodenheimer, P., et al. 1996, Icarus, 124, 62

Pont, F., Bouchy, F., Melo, C., et al. 2005, A&A, 438, 1123

Pont, F., Moutou, C., Bouchy, F., et al. 2006, A&A, 447, 1035

Ribas, I. 2003, A&A, 398, 239

Rice, W. K. M. & Armitage, P. J. 2003, ApJ, 598, L55

Robitaille, T. P., Whitney, B. A., Indebetouw, R., & Wood, K. 2007, ApJS, 169, 328

Ryabchikova, T., Piskunov, N., Kurucz, R. L., et al. 2015, Phys. Scr, 90, 054005

Sahlmann, J., Ségransan, D., Queloz, D., et al. 2011, A&A, 525, A95

Scott, N. J. & Howell, S. B. 2018, in Society of Photo-Optical Instrumentation Engineers (SPIE) Conference Series, Vol. 10701, Optical and Infrared Interferometry and Imaging VI, 107010G

Shporer, A., Zhou, G., Vanderburg, A., et al. 2017, ApJ, 847, L18

Siverd, R. J., Beatty, T. G., Pepper, J., et al. 2012, ApJ, 761, 123

Skrzypek, N., Warren, S. J., & Faherty, J. K. 2016, A&A, 589, A49

Southworth, J. 2011, MNRAS, 417, 2166

Spiegel, D. S., Burrows, A., & Milsom, J. A. 2011, ApJ, 727, 57

Stamatellos, D. 2015, ApJ, 810, L11

Tal-Or, L., Mazeh, T., Alonso, R., et al. 2013, A&A, 553, A30

Telting, J. H., Avila, G., Buchhave, L., et al. 2014, Astronomische Nachrichten, 335, 41

Toomre, A. 1964, ApJ, 139, 1217

Torres, G., Andersen, J., & Giménez, A. 2010, A&A Rev., 18, 67

Tremblin, P., Chabrier, G., Mayne, N. J., et al. 2017, ApJ, 841, 30

Triaud, A. H. M. J. 2018, The Rossiter-McLaughlin Effect in Exoplanet Research, 2

Triaud, A. H. M. J., Hebb, L., Anderson, D. R., et al. 2013, A&A, 549, A18

Triaud, A. H. M. J., Martin, D. V., Ségransan, D., et al. 2017, A&A, 608, A129

Triaud, A. H. M. J., Queloz, D., Bouchy, F., et al. 2009, A&A, 506, 377

Udry, S., Mayor, M., & Queloz, D. 1999, in Astronomical Society of the Pacific Conference Series, Vol. 185, IAU Colloq. 170: Precise Stellar Radial Velocities, ed. J. B. Hearnshaw & C. D. Scarfe, 367

Valenti, J. A. & Piskunov, N. 1996, A&AS, 118, 595

Vanderburg, A. & Johnson, J. A. 2014, PASP, 126, 948

von Boetticher, A., Triaud, A. H. M. J., Queloz, D., et al. 2017, A&A, 604, L6

Vorobyov, E. I. & Elbakyan, V. G. 2018, A&A, 618, A7

Weiss, L. M., Marcy, G. W., Rowe, J. F., et al. 2013, ApJ, 768, 14

Whitworth, A. P. 2018, Brown Dwarf Formation: Theory, 95

Winn, J. N. 2010, Exoplanet Transits and Occultations, ed. S. Seager (University of Arizona Press), 55–77

Winn, J. N., Holman, M. J., Henry, G. W., et al. 2007, AJ, 133, 1828

Zahn, J. P. & Bouchet, L. 1989, A&A, 223, 112

Zechmeister, M. & Kürster, M. 2009, A&A, 496, 577

Zhou, G., Bakos, G. Á., Bayliss, D., et al. 2019, AJ, 157, 31

Zhou, G., Bayliss, D., Hartman, J. D., et al. 2014, MNRAS, 437, 2831

[1] Chalmers University of Technology, Department of Space, Earth and Environment, Onsala Space Observatory, SE-439 92 Onsala, Sweden. e-mail: carina.persson@chalmers.se

[2] Institute of Planetary Research, German Aerospace Center (DLR), Rutherfordstrasse 2, D-12489 Berlin, Germany

[3] Lund Observatory, Department of Astronomy & Theoretical Physics, Lund University, Box 43, SE-221 00 Lund, Sweden

[4] Leiden Observatory, University of Leiden, PO Box 9513, 2300 RA, Leiden, The Netherlands

[5] Thüringer Landessternwarte Tautenburg, D-07778 Tautenburg, Germany

[6] Instituto de Astrofísica de Canarias (IAC), 38205 La Laguna, Tenerife, Spain

[7] Departamento de Astrofísica, Universidad de La Laguna, 38206 La Laguna, Tenerife, Spain

[8] Dipartimento di Fisica, Università di Torino, via Pietro Giuria 1, I-10125, Torino, Italy

[9] Department of Astronomy, The University of Tokyo, 7-3-1 Hongo, Bunkyo-ku, Tokyo 113-0033, Japan

[10] Department of Astronomy and McDonald Observatory, University of Texas at Austin, 2515 Speedway, Austin, TX 78712, USA

[11] Department of Earth and Planetary Sciences, Tokyo Institute of Technology, 2-12-1 Ookayama, Meguro-ku, Tokio, Japan

[12] Rheinisches Institut für Umweltforschung an der Universität zu Köln, Aachener Strasse 209, 50931 Köln, Germany

[13] Stellar Astrophysics Centre, Department of Physics and Astronomy, Aarhus University, Ny Munkegade 120, DK-8000 Aarhus C

[14] Department of Astronomy, The Ohio State University, 140 West 18th Ave., Columbus, OH 43210 USA

[15] Sub-department of Astrophysics, Department of Physics, University of Oxford, Oxford OX1 3RH, UK

[16] Department of Astrophysical Sciences, Princeton University, 4 Ivy Lane, Princeton, NJ, 08544, USA

[17] Institute für Physik, Geophysik, Astrophysik und Meteorologie, Karl-Franzens Universität Graz, Univ.-Platz 5, 8010 Graz, Austria

[18] Astronomy Department and Van Vleck Observatory, Wesleyan University, Middletown, CT 06459, USA

[19] Department of Physics and Kavli Institute for Astrophysics and Space Research, MIT, Cambridge, MA 02139, USA

[20] National Astronomical Observatory of Japan, NINS, 2-21-1 Osawa, Mitaka, Tokyo 181-8588, Japan

[21] Astronomical Institute, Czech Academy of Sciences, Fričova 298, 25165, Ondřejov, Czech Republic

[22] Astrobiology Center, NINS, 2-21-1 Osawa, Mitaka, Tokyo 181-8588, Japan

[23] Center for Astronomy and Astrophysics, TU Berlin, Hardenbergstr. 36, 10623 Berlin, Germany

[24] JST, PRESTO, 7-3-1 Hongo, Bunkyo-ku, Tokyo 113-0033, Japan

[25] Department of Earth, Atmospheric and Planetary Sciences, MIT, 77 Massachusetts Avenue, Cambridge, MA 02139, USA

[26] Institut de Ciències de l'Espai (ICE, CSIC), Campus UAB,C/ de Can Magrans s/n, E-08193 Bellaterra, Spain

[27] Institut d'Estudis Espacials de Catalunya (IEEC), C/ Gran Capità 2-4, E-08034 Barcelona, Spain

[28] Department of Theoretical Physics and Astrophysics, Masaryk University, Kotlářská 2, 61137 Brno, Czech Republic

[29] Astronomical Institute, Faculty of Mathematics and Physics, Charles University, Ke Karlovu 2027/3, 12116 Prague, Czech Republic

Table A.1: FIES RV measurements of EPIC 212036875.

BJD$_{TDB}$[a]	RV	
(-2 450 000.0)	(km s^{-1})	(km s^{-1})
FIES 1	Value	Error
8218.479167	-27.0655	0.0490
8220.404275	-18.5041	0.0458
8221.487928	-16.6310	0.0403
8222.391892	-19.6053	0.0523
8233.440969	-24.5166	0.0364
8235.385185	-21.1938	0.0465
FIES 2		
8245.450230	-22.8664	0.0877
8246.452557	-17.8474	0.0563
8247.446950	-17.0289	0.0730
FIES 3		
8251.403981	-18.6691	0.0357
8252.445391	-16.6940	0.0259
8253.439344	-19.7521	0.0260
8257.445193	-16.6979	0.0259
8258.437890	-18.8870	0.0202
8260.434739	-26.0322	0.0294
8261.435608	-20.1255	0.0259
8518.672339	-26.9764	0.0401
8522.638533	-22.1673	0.0255
8523.662787	-27.2661	0.0228
8524.698470	-22.4489	0.0242
8539.620870	-25.9885	0.0264
8540.645300	-19.9479	0.0337
8541.620968	-16.8566	0.0251

Notes. [a] Barycentric Julian day in barycentric dynamical time.

Appendix A: Additional Figures and Tables

Appendix B: Formation by gravitational instability

Given current uncertainties in both the initial masses of fragments formed by gravitational instability, and their subsequent growth and migration (Kratter & Lodato 2016; Fletcher et al. 2019), we evaluate the prospects for formation by disc instability using simple analytical prescriptions. We use the disc model of Ida et al. (2016), where the disc structure is determined by the viscosity, α, and the mass flux through the disc, $\dot{M}_{disc}$. We evaluate at which radii it is Toomre unstable, and if so, whether the mass of EPIC 212036875b is consistent with the expected fragment mass according to Eq. 49 in Kratter & Lodato (2016). The fragment masses are shown in Figure B.1. A self-gravitating disc maintains a viscosity $\alpha > 0.01$, while Class I YSOs (Young Stellar Objects) and FUORs (FU Orionis stars) have mass accretion rates up to a few times 10^{-5} (Robitaille et al. 2007; Gramajo et al. 2014). In these parameter ranges, our model forms fragments of several tens of Jupiter masses at > 10 AU, in agreement with previous works.
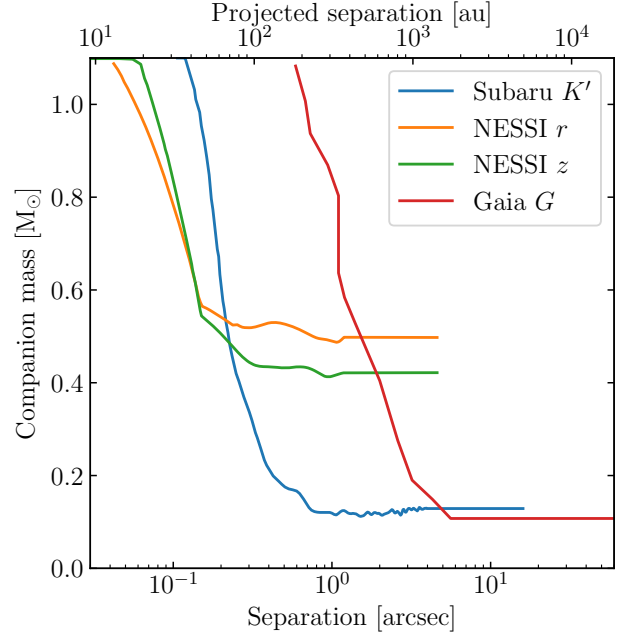

Fig. A.1: Limits of companion masses as a function of separation in arcsec and projected separation computed with the Baraffe et al. (2015) models for our NESSI and Subaru imaging, and the Gaia 50% detectability limit from Brandeker & Cataldi (2019).
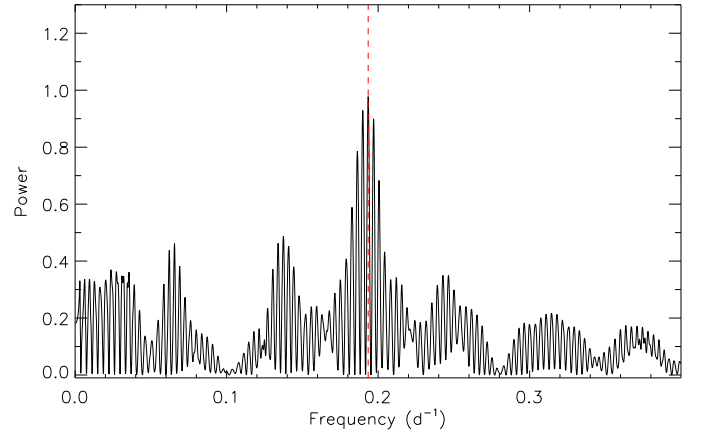

Fig. A.2: Generalised Lomb-Scargle periodogram of the combined FIES RVs. The red dashed line marks the orbital frequency of the brown dwarf. Note the presence of the 1-year aliases symmetrically distributed around the orbital frequency.
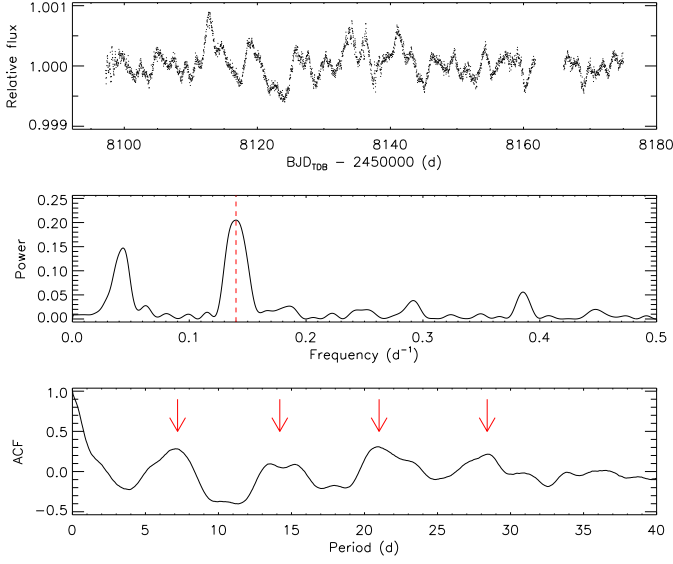
Fig. A.3: *Upper panel*: *K2* light curve of EPIC 212036875 following the removal of the in-transit data-points and the division by the best-fitting 4th-order cubic spline. *Middle panel*: GLS periodogram of the light curve. The red dashed line marks the peaks at the rotation period of the star (~7 days). *Lower panel*: ACF of the light curve. The red arrows mark the rotation period and its first three harmonics.
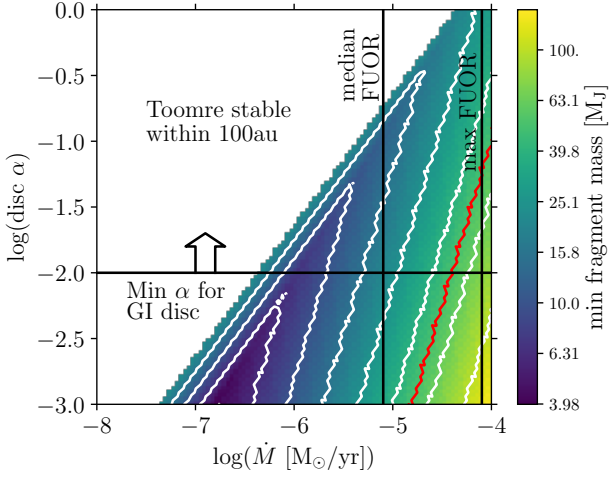

Fig. B.1: Formation of EPIC 212036875b by gravitational instability in a protoplanetary disc. The contour plot shows the minimum mass of a fragment arising from disc instability, as a function of the disc's viscosity and accretion rate. The red line marks masses equal to the observed mass of EPIC 212036875b. The horizontal black line marks the minimum α that a gravitationally unstable disc will generate, while the vertical black lines mark the median and maximum accretion rates for FUOR discs found by Gramajo et al. (2014). Discs in the white region to the left are gravitationally stable and hence do not form any fragments.